

Chapter 4

Inclusive Alpha production for ${}^6\text{Li}+{}^{51}\text{V}$ system

4.1 Introduction

4.2 Experimental details

4.3 Experimental Energy and Angular Distribution Spectra

4.4 Theoretical analysis

4.4.1 Statistical Model Calculation

4.4.2 CDCC Calculations

4.4.3 CRC Calculations

4.4.3.1 1-n transfer

4.4.3.2 1-p transfer

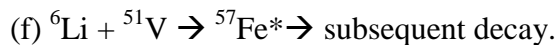
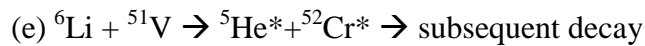
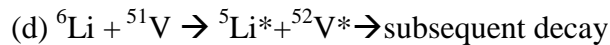
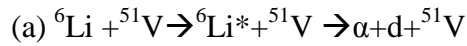
4.4.3.3 d-cluster transfer

4.5 Systematic studies

4.6 Summary and Conclusion

4.1 Introduction

The breakup of Weakly Bound Projectiles (WBP) having cluster structure (${}^6\text{Li}\rightarrow\alpha+d$) in the target field influence is a well-studied phenomenon [1, 2, 3]. Weakly bound projectile (WBP) heavy ion reactions undertake transfer and breakup apart from other reaction channels near the Coulomb barrier. For WBP with cluster structures such as ${}^{6,8}\text{Li}$, ${}^{6,7}\text{Li}$, and ${}^{7,9}\text{Be}$, several investigations have demonstrated the increased α -production in contrast to complimentary elements, and the underlying mechanism for the phenomenon continues to be intriguing today. [1, 4, 5, 6]. In order to understand WBP break up, inclusive breakup cross sections are measured using the total α -yield. Inclusive α -production incorporates distinct reaction mechanisms viz. direct/sequential breakup, compound nuclear evaporation, nucleon transfer followed by breakup; incomplete fusion or transfer of a cluster. Thus considering probable channels, system can go through processes like



The larger yields of alpha indicate the existence of other channels also apart from the breakup process [1, 7].

4.2 Experimental details

The experimental work was performed using a General Purpose Scattering Chamber (GPSC) of 14UD Pelletron-LINAC accelerator facility at TIFR, Mumbai. The measurement was done using a ${}^6\text{Li}^{3+}$ ion beam bombarded with energies 14, 20, 23, 26 MeV between current range 5-28 nA on self-supported 1.17 mg/cm^2 thick ${}^{51}\text{V}$ target. A rectification of beam energies for half thickness of target were performed during scrutiny. This accounts for a deduction of $\sim 280\text{ keV}$ to $\sim 400\text{ keV}$ for 26 MeV to 14 MeV energy range. Thus corrected beam energies are 13.6, 19.7, 22.7, and 25.7 MeV. The detection of charged particles involved was done with the help of silicon surface barrier detectors on $\Delta E+E$ telescope arrangement covering 14° to 170° angular range. A typical $\Delta E-E$ 2-D plot is shown in figure 4.1 at energy $E_{\text{lab}}=19.7\text{ MeV}$ and $\theta_{\text{lab}}=30^\circ$. The statistical errors were $\approx 1\%$ in forward angle to $\approx 10\%$ above $\theta_{\text{lab}}=70^\circ$. The data were registered and analyzed handling Linux-based data acquisition system LAMPS [8].

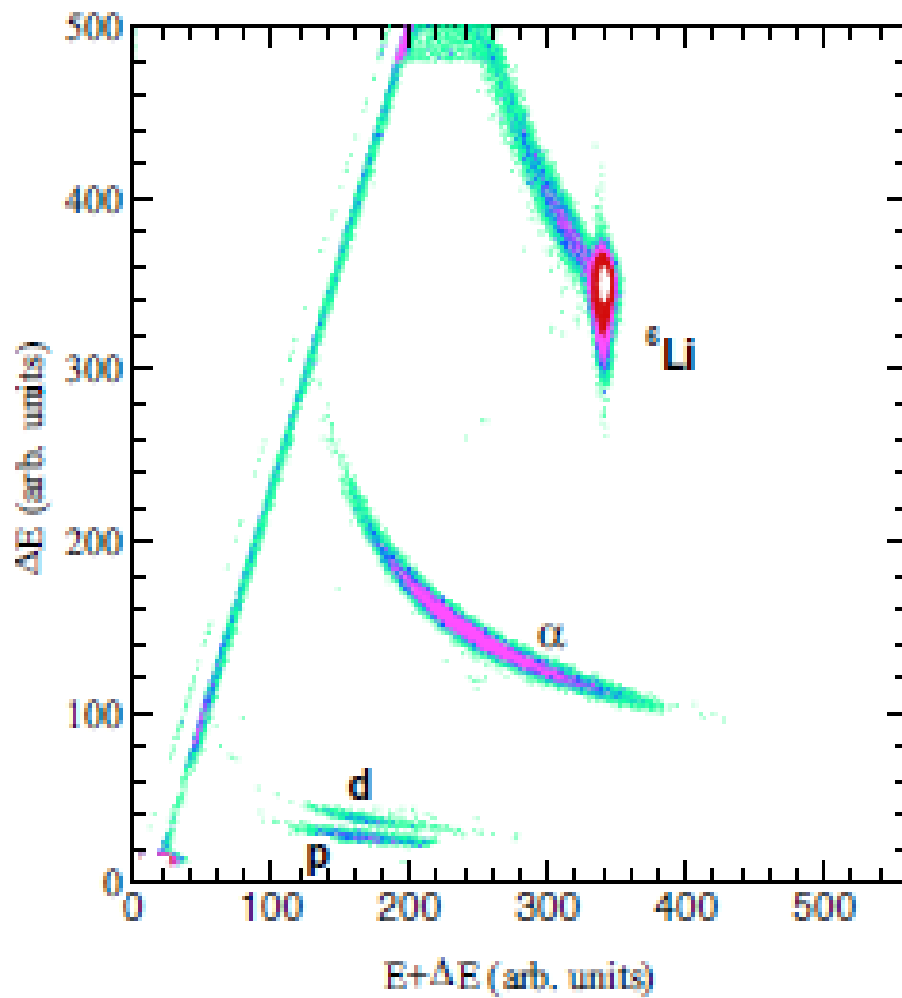


Figure 4.1: Particle ΔE -($E+\Delta E$) spectrum at $E_{lab}=19.7\text{MeV}$, $\theta_{lab}=30^\circ$, for the system ${}^6\text{Li}+{}^{51}\text{V}$.

4.3 Experimental Energy and Angular Distribution Spectra

The maximum output of an alpha particle may be found at the energy where the alpha particle's kinetic energy of each nucleon is approximately equivalent to incoming particle's energy. Approximately 2/3 of the incoming ${}^6\text{Li}$ energy will be produced at most, through the alpha particle created following the disintegration of ${}^6\text{Li}$. Figures 4.2 and 4.3 show the energy spectrum for 25.7 MeV and 19.7 MeV, respectively, at various angles. In order to demonstrate the involvement of compound nuclei in addition to direct nuclear reactions, these experimental energy spectra incorporate the outcomes of statistical model calculation. The direct contribution was obtained by subtracting the compound nuclear part from measured α production. It is clear from figures that while the front angles and grazing angles exhibit the contribution from various direct channels, the backward angles exhibit the almost exclusive contribution from evaporation and thus possess good agreement between the compound nuclear contribution and experimentally determined energy spectra. Additionally, for lower incidence energies, the non-compound reaction contribution decreases compared to higher ones. The alpha energy spectrum was integrated for each angle. The energy integrated differential cross section was calculated assisting following equation:

$$\frac{d\sigma}{d\omega} = \frac{Y_{incl}}{Y_{el}} X \frac{d\sigma_{el}}{d\omega} \quad (4.1)$$

To abolish the effect of error in target thickness, monitor counts, and dead time either in the detector or acquisition system, we make use of Y_{el} as a normalizing factor for each alpha group

at the same angle. $d\sigma_{el}/d\omega$ is an elastic scattering cross section, and it minimizes the systematic error. Y_{el} and Y_{incl} are elastic and alpha yields, respectively. Figure 4.4 plots angular distribution of α -particle production cross section. The level density and diffuseness parameters for evaporation calculations were fixed to match the energy spectrum at back angle.

To secure angle integrated cross section (i.e. total α -breakup), the differential angular cross section of the difference of (direct + compound) reaction to compound reaction was fitted to the Gaussian shape to $(d\sigma/d\Omega) \times 2\pi \sin \theta$ distribution. Employing the following equation the integral α -production cross section was computed -

$$\sigma = \int_0^{2\pi} d\varphi \int_0^\pi \frac{d\sigma(\theta)}{d\Omega} \sin \theta d\theta \quad (4.2)$$

The error caused by fitting procedure is weighted error with goodness of fits. The total error shown are the statistical and fitting errors. Table 4.1 demonstrates experimental total α cross section with errors.

4.4 Theoretical analysis

4.4.1 Statistical Model Calculation

A statistical model PACE assisted to identify the presence of the compound nuclear part to total α -production cross section [9]. The excitation energy resemblance at backward angles at 26MeV energy was obtained with a level density parameter ($A/10$) and diffusion parameter 4 with a level density as prescribed by Ignatyuk et al.[10]. The energy spectra at different angles for energies

25.7 MeV and 19.7 MeV are demonstrated in figures 4.2 and 4.3 respectively. Figure 4.4 illustrates trend for α -production brought on by the compound nucleus evaporation process.

4.4.2 Coupled Reaction Channel Calculations (CDCC)

The detailed description about the CDCC calculations are given in chapter 2 in section 2.5.4.2. The calculation of non-capture breakup and elastic breakup cross section was done by CDCC in code FRESCO version 3.1 [11, 12]. The two body cluster form of ${}^6\text{Li}$ is considered. The continuum above the breakup threshold of (${}^6\text{Li}\rightarrow\alpha+d$) was discretized into momentum bins of width $\Delta k = 0.1 \text{ fm}^{-1}$ and trimmed at max energy of 9.25 MeV. Ahead of this, individual continuum or resonance state was binned into 40 equal k bins. The relative orbital angular momentum of $L=0, 1, 2, 3$ and $1+, 2+, 3+$ resonances for $L=2$ with experimental widths at 2.186, 4.312, and 5.65 MeV, respectively were included. The binding potentials for the $\alpha+d$ cluster were incorporated from reference [13]. The resonance potentials were deduced from

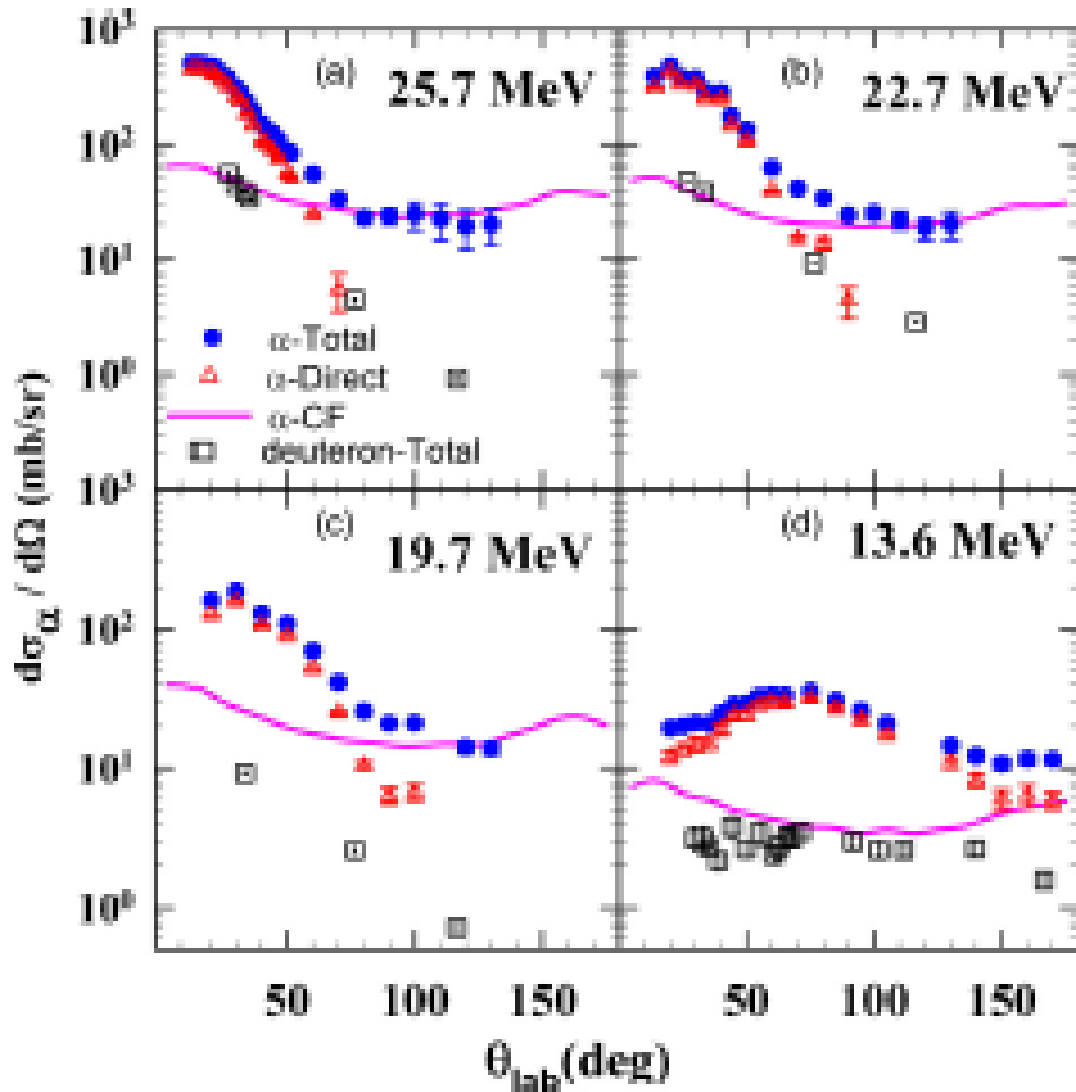


Figure 4.4: Energy integrated angular distribution of α -particles at various energies (a) 25.7 MeV, (b) 22.7 MeV, (c) 19.7 MeV, and (d) 13.6 MeV at ${}^6\text{Li}+{}^{51}\text{V}$. The solid circles indicate the total α cross section, the solid line is representative of compound nuclear reaction, and the hollow triangle represents direct or non-compound (total-compound) contributions. The total deuteron cross section is included by hollow squares.

reference [14]. The cluster folding potentials for $\alpha+{}^{51}\text{V}$ and $\text{d}+{}^{51}\text{V}$ were generated from reference [15, 16] at corresponding energies. Thus obtained breakup cross sections are recorded in Table 4.1. Figure 4.7 illustrates plots for angular distribution of above.

4.4.3 Coupled Reaction Channels (CRC) Calculations

To comprehend the internal characteristics of nuclei, the transfer and inelastic reaction channels are useful resources. Thus to explore the single particle structure of nuclei and to extract spectroscopic factors of them, transfer reactions studies are taken care of. To solve the purpose, we have studied 1n, 1p, and 1d transfer leading to, their cross sections and thus their contributions to direct α -production. The coupling between parent and daughter nucleus may be from various bound or excited states. To calculate CRC few physical parameters are needed like (a) structural information of participating nuclei; (b) optical potentials for incoming and outgoing distorted waves; (c) a unique identification of overlapping function, which normally represent single particle states in a Wood-Saxon potential, which is recreating a bound state by altering the depth of the binding potential; (d) a spectroscopic factor which signifies the probability of finding a core state within a composite state. In process, the excitation energy for a given channel affects the coupling to discrete or continuous channels. Incoming channels optical potential for were deduced from the elastic scattering data [14].

4.4.3.1 1-n transfer

When the breakup of the projectile takes place such that ${}^6\text{Li} \rightarrow {}^5\text{Li} (p+\alpha) + n$ leads to reaction ${}^{51}\text{V}({}^6\text{Li}, {}^5\text{Li}){}^{52}\text{V}$ then 1-n transfer takes place to contribute α -production. The projectile and target bound state potentials were assumed to have a Wood-Saxon form factor with reduced radii $r_0=1.25$ fm and diffuseness $a=0.65$ fm. The incorporation of spin-orbit interaction was done with a standard depth of 6 MeV. The depth of real potential was set free to vary to reproduce experimental neutron binding energies. The post form of reaction was used and finite range transfer approximation were used in FRESKO [11]. Spectroscopic factors for projectile were involved from reference [15] and for targets were included from reference [16]. The calculations incorporated $2p_{3/2}$, $1f_{5/2}$, $2p_{1/2}$, and $1g_{9/2}$ orbits of model space of ${}^{52}\text{V}$ by assuming $1f_{7/2}$ as the terminating subshell in the ground state. The continuum coupling above the neutron bound state was contemplated with the angular momentum of $L=0 \rightarrow 5 \hbar$ and utilizing equal linear momentum bins up to ≈ 15 MeV for energies. A schematic diagram incorporating of two way coupling scheme of states and target overlaps is shown in figure 4.5. The resultant contribution from the 1-n transfer is given in Table 4.1 and its total angular distribution is shown in figure 4.7.

4.4.3.2 1-p transfer

The breakup of the projectile occurs so that the reaction takes place and thus 1-p transfer contributes to α -production. The spectroscopic factors for target were included from reference [17]. The calculations incorporated p transfer to $1f_{7/2}$, $2p_{3/2}$ orbits of model space of ${}^{52}\text{Cr}$. The

spectroscopic factors were assigned one for higher states' contribution up to 9.5 MeV. The continuum coupling up to 12 MeV above the bound state were contemplated to give a small contribution. A schematic diagram incorporating of two way coupling scheme of states and target overlaps is shown in figure 4.6. The resultant contribution from 1-p transfer is recorded in Table 4.1 and its total angular distribution is shown in figure 4.7.

4.4.3.3 d-cluster transfer

The 1d transfer takes place to contribute α -production when the breakup of the projectile takes place to reaction ${}^{51}\text{V}({}^6\text{Li}, {}^4\text{He}){}^{53}\text{Cr}$. The spectroscopic factors for the projectile and target were taken as one. This reaction has a high Q -value, $Q = 14.745$ MeV thus transfer to low-lying discrete states have unaccountably less contribution. Therefore, the continuum coupling of ${}^{53}\text{Cr}$ above deuteron binding energy was contemplated with the angular momentum of $L=0 \rightarrow 7 \hbar$ and utilizing equal liner momentum bins with width $\Delta k = 0.1 \text{ fm}^{-1}$ up to ≈ 12 MeV for energies. The cross section of the resultant contribution from the 1-d transfer is recorded in Table 4.1 and its total angular distribution is shown in figure 4.7.

Figure 4.7 shows the total contribution from both Non- Capture Breakup (NCBU) and transfer channels. Their sum is represented by Tr+NCBU (black dashed line). The ICF α contribution were added by multiplying (Tr+NCBU) $(\sigma_{\alpha}^{\text{cal}} / \sigma_{\alpha}^{\text{cal}} - \sigma_{\alpha}^{\text{ICF}})$ shown in the orange solid line in the figure. It can be seen that the sum agrees very well with the experimental data and the tiny difference might be due to the uncertainties in spectroscopic factors as well as consideration of the limited number of states in transfer calculation. The estimation of α - production from breakup fusion or incomplete fusion (ICF) was designed as suggested by Jha *et al.*[18]

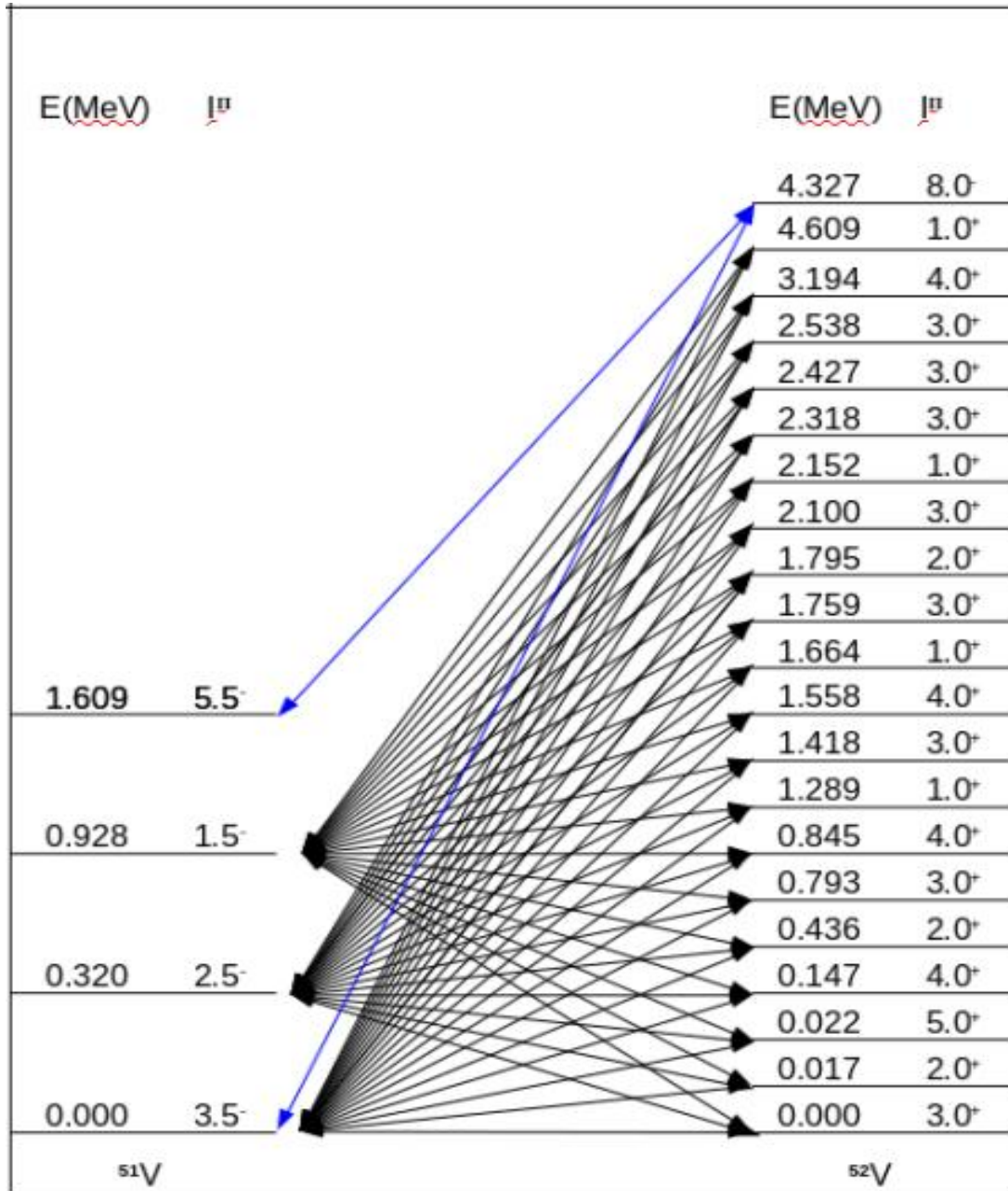


Figure 4.5: Schematic diagram of coupling states included for Coupled Reaction Channel Calculations (CRC) for 1-n transfer.

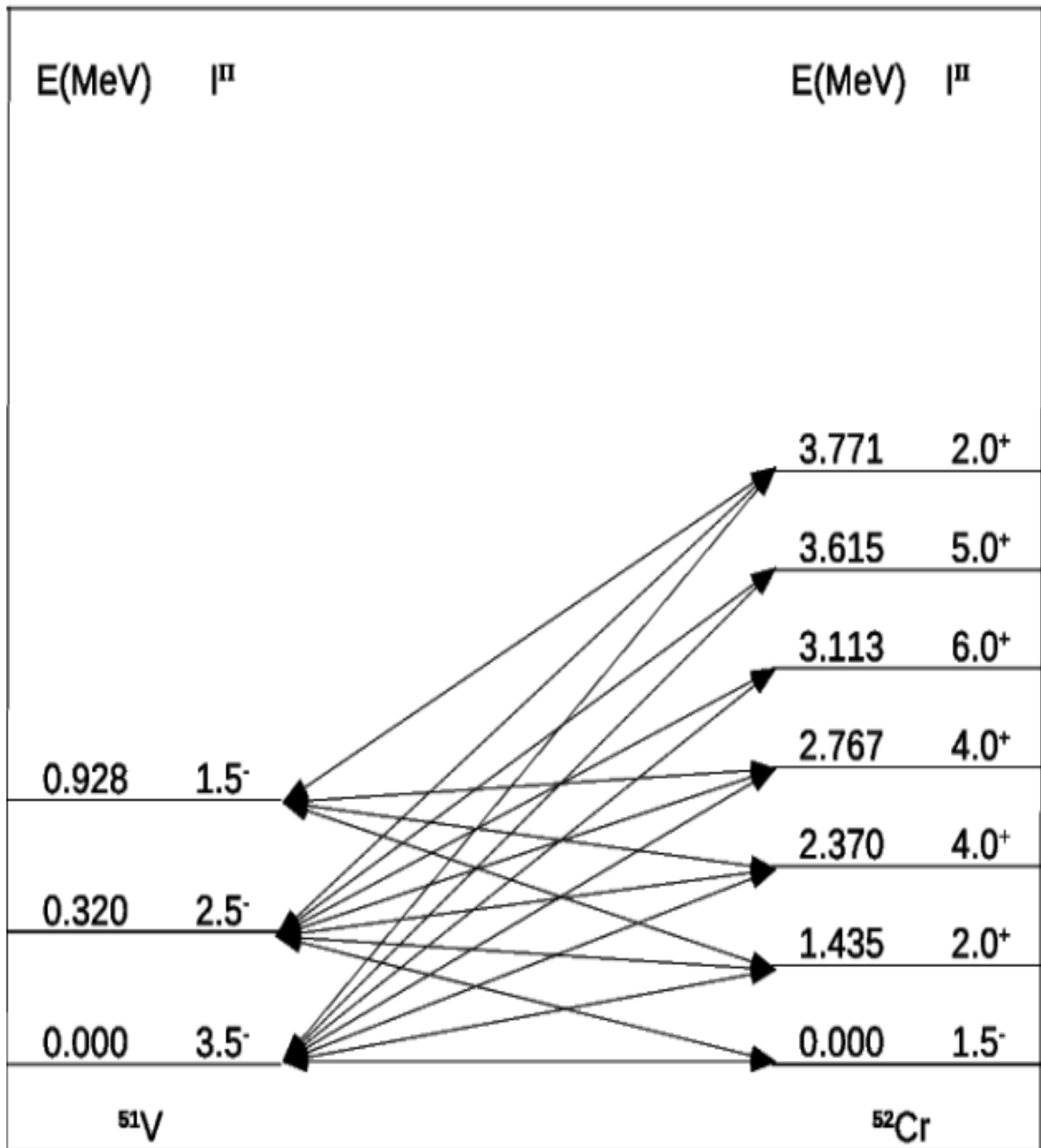


Figure 4.6: Schematic diagram of coupling states included for Coupled Reaction Channel Calculations (CRC) for 1-p transfer.

Table 4.1

Experimental direct α production ($\sigma_{\alpha}^{\text{direct}}$) and total deuteron production cross sections (σ_{d}) deduced from integral of measured angular distributions, calculated cross sections for α production by compound nuclear reactions ($\sigma_{\alpha}^{\text{CN}}$), noncapture breakup ($\sigma_{\alpha}^{\text{NCBU}}$), $1n$ transfer (σ_{1n}^{T}), $1p$ transfer (σ_{1p}^{T}), $1d$ transfer (σ_{1d}^{T}), ICF ($\sigma_{\alpha}^{\text{ICF}}$), and total calculated direct α production ($\sigma_{\alpha}^{\text{cal.}}$). Transfer calculations are performed using FRESKO and compound nuclear calculations are done with PACE code. The complete fusion cross sections given by PACE are denoted by $\sigma_{\text{pace}}^{\text{CF}}$

E_{lab}(MeV)	25.7	22.7	19.7	13.6
$\sigma_{\alpha}^{\text{direct}}$ (mb)	510±46	490±68	403±11	239±8
σ_{d} (mb)	136±27	144±38		3±7
$\sigma_{\alpha}^{\text{CN}}$ (mb)	387	304	230	54
$\sigma_{\text{pace}}^{\text{CF}}$ (mb)	1056	963	826	279
$\sigma_{\alpha}^{\text{NCBU}}$ (mb)	62	58	52	25
σ_{1n}^{T} (mb)	43	36	25	24
σ_{1p}^{T} (mb)	16	16	15	10
σ_{1d}^{T} (mb)	61	61	56	42
$\sigma_{\alpha}^{\text{ICF}}$ (mb)	277	253	217	73
$\sigma_{\alpha}^{\text{cal.}}$ (mb)	459	424	365	174

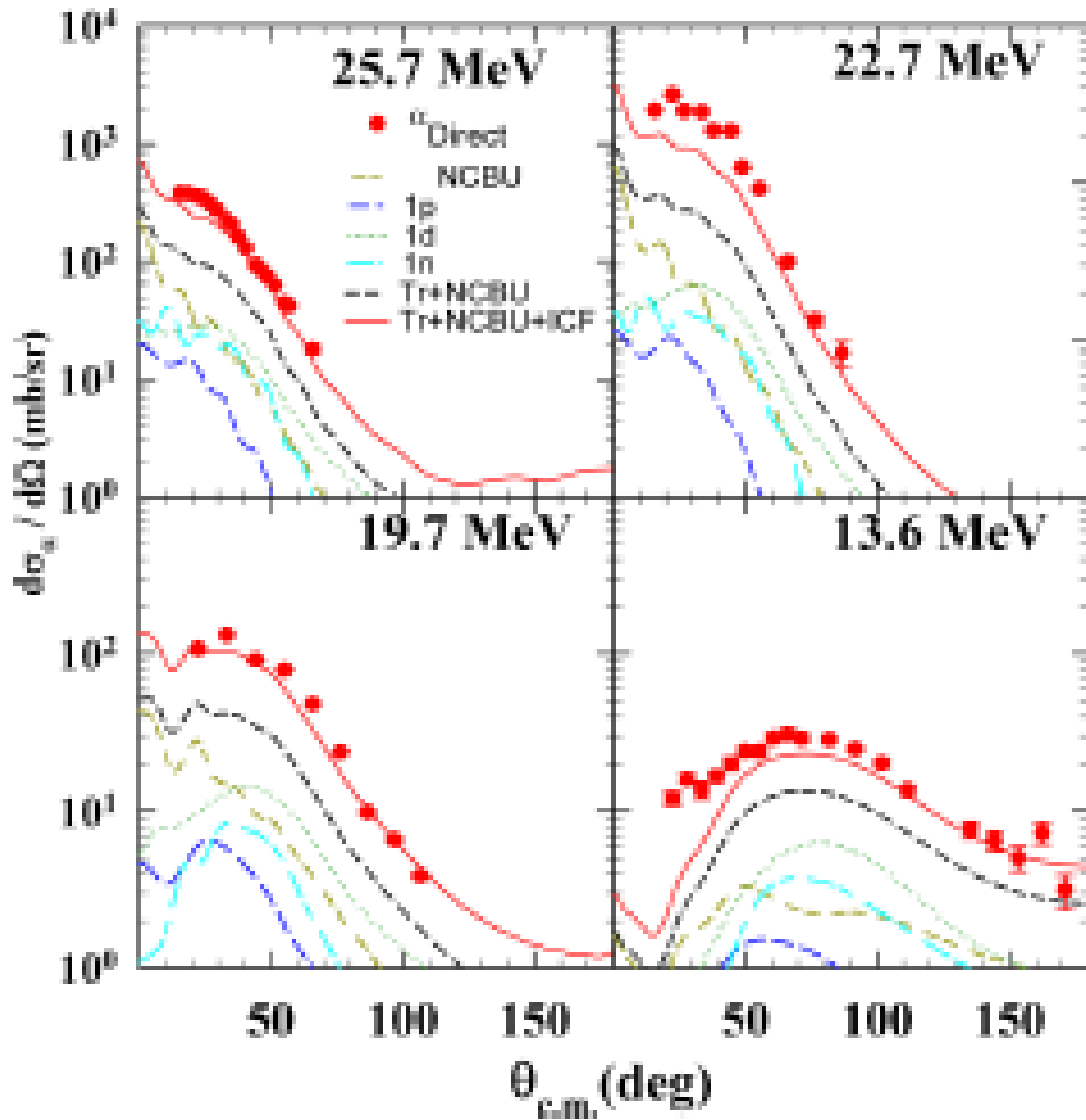


Figure 4.7: The contribution of several possible reaction channels to direct α production viz. non-capture breakup (dark yellow dashed line), 1 p transfer (blue dashed line), 1 n transfer (cyan dashed line), 1 d transfer (green dotted line), transfer + Non-capture breakup (NCBU) (black dashed line), and Incomplete fusion +transfer +NCBU is represented by the red solid line. The experimental inclusive direct α cross section is depicted by solid red circles.

4.5 Systematic studies

For lighter to heavier mass range targets with ${}^6\text{Li}$, a systematized study of direct α production for numerous targets was carried out. The reduction method proposed by Gomes et al. [19] was involved for vanishing of geometrical effects of participating nuclei quantities such as cross section. The reduction procedure scales the cross section to $\sigma_R/(A_P^{(1/3)} + A_T^{(1/3)})^2$ and energy to be scaled as $E_{c.m.}(A_P^{(1/3)} + A_T^{(1/3)}) / Z_P Z_T$ here T, P stand for target, projectile respectively, σ_R for cross section, Z stand for mass/atomic number and E for the energy of the projectile. . Figure 4.8 shows the variation of the direct contributions with a universal trend. Saturation above the barrier can be noticed and a considerable difference in contribution from variety of targets can be seen. Various transfer channels contribute to direct α thus nuclear structure has an impact on these. A suppression in reduced cross section of lighter and middle mass targets can be seen but not in heavier mass targets. A systematic study of relative cross sections of alpha and deuteron was also carried out and the ratio is plotted in the figure 4.9. The cross sections for the present system, target ${}^{51}\text{V}$, ${}^{59}\text{Co}$, ${}^{118}\text{Sn}$, ${}^{238}\text{U}$ are taken from direct observations whereas for ${}^{124}\text{Sn}$ and ${}^{159}\text{Tb}$ drawn from ICF residue cross sections. The ratio gives a hint of more reaction channels for α -production (such as breakup, breakup fusion, d-transfer, n and p transfer followed by a breakup, etc.) in comparison to deuteron production (such as α -transfer, breakup, and breakup fusion, etc.).

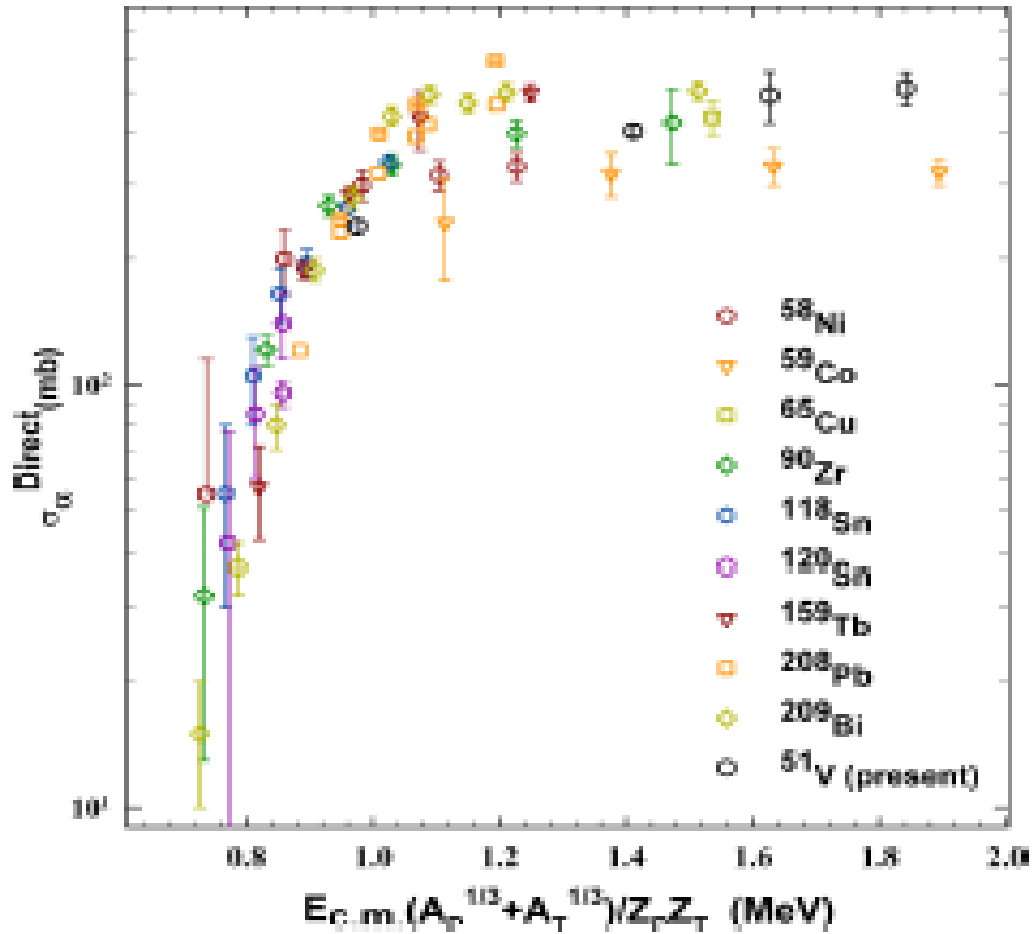


Figure 4.8: Experimentally deduced direct α -particle cross section for ${}^6\text{Li}$ with various targets. The cross section for different targets are extracted from the literature ${}^{58}\text{Ni}$, ${}^{118}\text{Sn}$, ${}^{128}\text{Sn}$ [20], ${}^{59}\text{Co}$ [3], ${}^{65}\text{Cu}$ [21], ${}^{90}\text{Zr}$ [22], ${}^{159}\text{Tb}$ [23], ${}^{208}\text{Pb}$ [24,25], and ${}^{209}\text{Bi}$ [26]. The present work for the system ${}^6\text{Li}+{}^{51}\text{V}$ has been represented in black hollow circles.

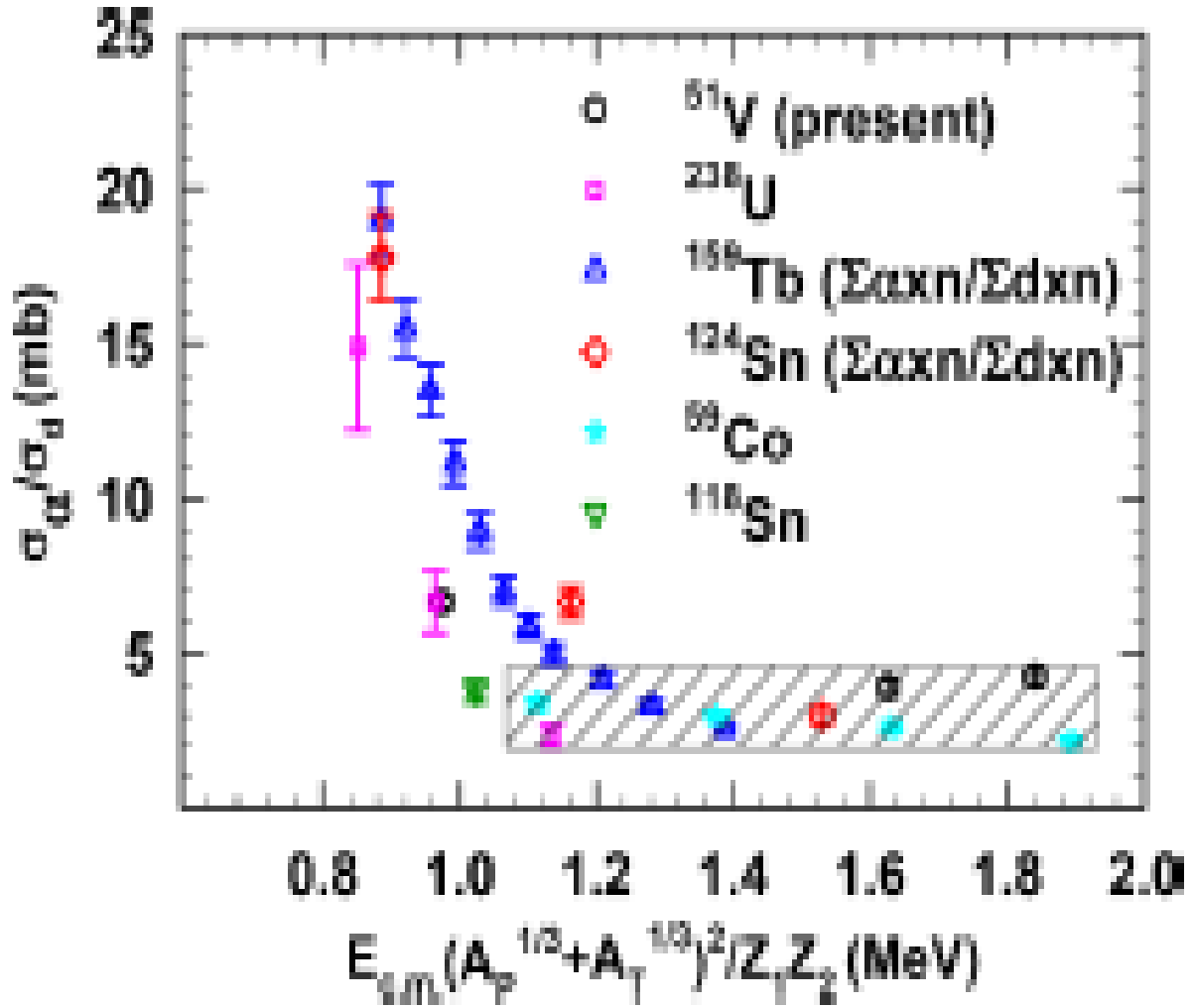


Figure 4.9: A ratio showing relative production of α - production cross section to deuteron production cross section for various targets around the Coulomb barrier. Experimental data have been included for targets ${}^{238}\text{U}$ [27], ${}^{124}\text{Sn}$ [28], ${}^{159}\text{Tb}$ [21], ${}^{59}\text{Co}$ [3], and ${}^{118}\text{Sn}$ [18].

Summary and Conclusion:

Experimental measurements of inclusive α - production probabilities over a large range of angles weakly bound projectile ${}^6\text{Li} + {}^{51}\text{V}$ system have been performed. The substantial α -particle production was remarked. The compound nucleus contribution to α -particle spectra was removed using statistical model estimations, leaving just the direct contributions. Different calculations were made to separate out the contribution from various channels viz. n, p, and d transfers using CRC calculations, non-capture breakup calculations using CDCC, and ICF (incomplete fusion) α assessments utilizing fusion cross sections. Further, summing the cross sections of all calculated channels is reproducing well the energy, angular distribution, and integral cross section. The higher Q value of deuteron transfer reaction is responsible for negligible contribution of transfer to discrete states and considerable contribution to continuum states. In case of p and n transfers, the transfer to continuum contributes to enhancement in cross section along with discrete states. As a result, the overall estimated direct α cross sections and the experimental cross section measurements correlate quite well. The fusion cross section was a tool to obtain the ICF cross sections. Direct α cross section depicts a global trend. Well, there is always a difference among different targets perhaps owing to structure effects during α production furnished by transfer channels. A relative study for α production to that of deuteron production is done for numerous targets nearby the Coulomb barrier and α production cross section is remarked significantly higher in comparison to the deuteron production cross section. This might be because of more reaction channels for α production and a different Coulomb barrier in the production of

deuterons. The ratio reaches saturation over the barrier energies most likely because of open channel number saturation.

References:

- [1] J. Lei and A. M. Moro, Phys. Rev. C **95**, 044605 (2017).
- [2] A. Pakou, N. Alamanos, A. Gillibert, M. Kokkoris, S. Kossionides, A. Lagoyannis, N. G. Nicolis, C. Papachristodoulou, D. Patiris, D. Pierrotsakou *et al.*, Phys. Rev. Lett. **90**, 202701 (2003).
- [3] F. A. Souza, C. Beck, N. Carlin, N. Keeley, R. L. Neto, M. M. de Moura, M. G. Munhoz, M. G. D. Santo, and A. A. P. Suaide, Nucl. Phys. A **821**, 36 (2009).
- [4] L. F. Canto, P. R. S. Gomes, R. Donangelo, J. Lubian, and M. S. Hussein, Phys. Rep. **596**, 1 (2015).
- [5] O. Sgouros, A. Pakou, D. Pierrotsakou, M. Mazzocco, L. Acosta, X. Aslanoglou, C. Betsou, A. Boiano, C. Boiano, D. Carbone *et al.*, Phys. Rev. C **94**, 044623(2016).
- [6] J. J. Kolata, V. Guimarães, and E. F. Aguilera, Eur. Phys. J. A **52**, 123 (2016).
- [7] A. Pal, S. Santra, D. Chattopadhyay, A. Kundu, A. Jhingan, P. Sugathan, B. K. Nayak, A. Saxena, and S. Kailas, Phys. Rev. C **99**, 024620 (2019).
- [8] A. Chatterjee, LAMPS: Linux Advanced Multiparameter System (2008), <https://www.tifr.res.in/~pell/lamps.html>.
- [9] A. Gavron, Phys. Rev. C **21**, 230 (1980).
- [10] A. V. Ignatyuk, G. N. Smirenkin, and A. S. Tishin, Sov. J. Nucl. Phys. **21**, 255 (1975).

- [11] I. J. Thompson, Comput. Phys. Rep. **7**, 167 (1988).
- [12] I. J. Thompson, FRESKO (2019), version FRES 3.1 [<http://www.fresco.org.uk/source/fres-v31.html>].
- [13] K. I. Kubo and M. Hirata, Nucl. Phys. A **187**, 186 (1972).
- [14] H. Kumawat, C. Joshi, V. V. Parkar, V. Jha, B. J. Roy, Y. S. Sawant, P. C. Rout, E. T. Mirgule, R. K. Singh, N. L. Singh *et al.*, Nucl. Phys. A **1002**, 121973 (2020).
- [15] S. Cohen and D. Kurath, Nucl. Phys. A **101**, 1 (1967).
- [16] O. Karban, J. England, D. Barker, M. Mannion, J. Nelson, C. Ogilvie, L. Potvin, L. Zybert, R. Zybert, N. Clarke *et al.*, Nucl. Phys. A **472**, 189 (1987).
- [17] F. Pellegrini, I. Filosofo, M. I. El Zaiki, and I. Gabrielli, Phys. Rev. C **8**, 1547 (1973).
- [18] V. Jha, V. V. Parkar, and S. Kailas, Phys. Rep. **845**, 1 (2020), and references therein.
- [19] P.R.S. Gomes, J. Lubian, I. Padron, R.M. Anjos, Phys. Rev. C **71** (2005) 01760.
- [20] K. Pfeiffer, E. Speth, and K. Bethge, Nucl. Phys. A **206**, 545 (1973).
- [21] A. Shrivastava, A. Navin, N. Keeley, K. Mahata, K. Ramachandran, V. Nanal, V. V. Parkar, A. Chatterjee, and S. Kailas, Phys. Lett. B **633**, 463 (2006).
- [22] H. Kumawat, V. Jha, V. V. Parkar, B. J. Roy, S. Santra, V. Kumar, D. Dutta, P. Shukla, L. M. Pant, A. K. Mohanty *et al.*, Phys. Rev. C **81**, 054601 (2010).
- [23] M. K. Pradhan, A. Mukherjee, S. Roy, P. Basu, A. Goswami, R. Kshetri, R. Palit, V. V. Parkar, M. Ray, M. Saha Sarkar *et al.*, Phys. Rev. C **88**, 064603 (2013).

Chapter 4: Inclusive Alpha production for ${}^6\text{Li}+{}^{51}\text{V}$ system

- [24] C. Signorini, M. Mazzocco, G. F. Prete, F. Soramel, L. Stroe, A. Andrighetto, I. J. Thompson, A. Vitturi, A. Brondi, M. Cinausero *et al.*, *Eur. Phys. J. A* **10**, 249 (2001).
- [25] C. Signorini, A. Edifizi, M. Mazzocco, M. Lunardon, D. Fabris, A. Vitturi, P. Scopel, F. Soramel, L. Stroe, G. Prete *et al.*, *Phys. Rev. C* **67**, 044607 (2003).
- [26] S. Santra, S. Kailas, V. V. Parkar, K. Ramachandran, V. Jha, A. Chatterjee, P. K. Rath, and A. Parihari, *Phys. Rev. C* **85**, 014612 (2012).
- [27] A. Pal, S. Santra, D. Chattopadhyay, A. Kundu, A. Jhingan, P. Sugathan, B. K. Nayak, A. Saxena, and S. Kailas, *Phys. Rev. C* **99**, 024620 (2019).
- [28] V. V. Parkar, S. K. Pandit, A. Shrivastava, R. Palit, K. Mahata, V. Jha, K. Ramachandran, S. Gupta, S. Santra, S. K. Sharma *et al.*, *Phys. Rev. C* **98**, 014601 (2018).

Chapter 4: Inclusive Alpha production for ${}^6\text{Li}+{}^{51}\text{V}$ system